Nezha-Mini: Design and Locomotion of a Miniature Low-Cost Hybrid Aerial Underwater Vehicle

Yuanbo Bi, *Graduate Student Member, IEEE*, Yufei Jin, *Graduate Student Member, IEEE*, Chenxin Lyu, *Graduate Student Member, IEEE*, Zheng Zeng, *Member, IEEE*, and Lian Lian, *Senior Member, IEEE*

***Abstract*—The distinct design concepts of the vehicles operating in air and water is one of the tremendous challenges that constrain the development of the hybrid aerial underwater vehicle (HAUV). This incompatibility consequently results in the enlarging volume and weight of the existing prototypes, as well as the unmatched maneuvering characteristics in both domains. This letter presented a novel miniaturized and lightweight HAUV, "Nezha-mini," which weighs 953 g and is only A4-scaled. Besides, the low cost and high modularity allow the convenient repair and remanufacturing. Nezha-mini reconciles the complete multi-domain maneuverability within 50 m aerially and 6 m underwater whilst sufficing for the rapid and stable cross-domain locomotion, which benefits from the selection and unique layout of the propulsion system, as well as our proposed multi-modal control strategy and the cross-domain triggering mechanism. The results of the field experiments are in good agreement with the dynamics simulation, demonstrating the performance of multi-domain locomotion in real environments. The preliminary exploration in this letter provides a referential solution for the miniaturization of the highly maneuverable HAUVs for practical applications and creates a feasible platform for the future clustering and networking of HAUVs.**

***Index Terms*—Hybrid aerial underwater vehicle, miniaturization, multi-modal control, cross-domain locomotion.**

I. Introduction

THE miniaturized and lightweight robot is attracting growing attention in robotics due to the preponderance of solid flexibility, concealment, and portability [1]. The miniature unmanned aerial vehicles (UAV) [2] and unmanned underwater vehicles (UUV) [3] have indispensable applications in their respective fields, such as cluster detection and formation cooperative operation [4]. In addition, the cases of cross-domain collaboration between UAV and UUV are also emerging rapidly [5].

Manuscript received November 16, 2021; accepted April 19, 2022. Date of publication May 20, 2022; date of current version May 31, 2022. This letter was recommended for publication by Associate Editor B. Duncan and Editor P. Pounds upon evaluation of the reviewers' comments. This work was supported in part by the National Natural Science Foundation of China under Grant 41706108, in part by the Shanghai Committee Science and Technology under Project 20dz1206600, in part by the Natural Science Foundation of Shanghai under Grant 20ZR1424800, and in part by the Shanghai Jiao Tong University Scientific and Technological Innovation Funds under Grant 2019QYB04. *(Corresponding author: Zheng Zeng.)*

The authors are with the School of Oceanography, Shanghai Jiao Tong University, Shanghai, Minhang District 200240, China (e-mail: biyuanbo@sjtu.edu.cn; 594786825@qq.com; lvchenxin@sjtu.edu.cn; zheng.zeng@sjtu.edu.cn; llian@sjtu.edu.cn).

This letter has supplementary downloadable material available at https://doi.org/10.1109/LRA.2022.3176438, provided by the authors.

Digital Object Identifier 10.1109/LRA.2022.3176438

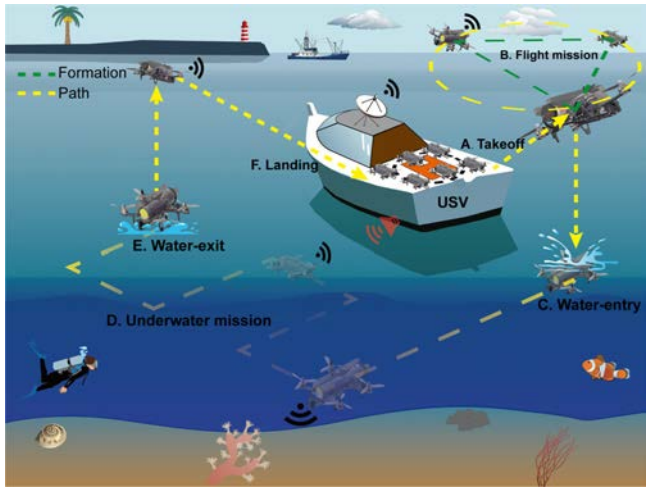

Fig. 1. Schematic of the cooperative operation of the unmanned system cluster. **A.** The HAUV formation takes off from the unmanned surface vessel (USV). **B.** The formation performs the flight mission on a preset path. **C.** The formation enters the water. **D.** The formation performs the underwater mission and communicates with the USV through the underwater acoustic. **E.** The formation leaves the water. **F.** Course reversal.

In the past decade, there have been attempts to bridge UAV and UUV to create hybrid aerial underwater vehicles (HAUV) with multiphase traversal capabilities [6]. Therefore, the miniaturized HAUV is a crucial link in the future development of HAUV and charts a desirable blueprint for the application scenarios of the multi-domain cooperative operation of heterogeneous unmanned vehicles as shown in Fig. 1.

Despite these prospective advantages, the miniaturized HAUV faces unique challenges and constraints. The fluid properties differ considerably between the two domains, that is, air and water. The relatively independent and mature configurations of the vehicles operating in both extreme domains can be non-intersecting or even contradictory during the integration, which is the inherent problem in the HAUV design process [7]. In order to ensure the capabilities of multi-modal locomotion, diversified propulsive strategies that consider the different physical constraints of both airborne and underwater environments are required, and the tradeoffs of performance are inevitable [8]. Moreover, in the trans-media process, the response frequency of the miniaturized HAUV is more severe when subjected to environmental disturbance than the existing normal-scale HAUV, and the disturbance amplitude that the miniaturized HAUV can

TABLE I
COMPARISON OF THE SIZE, WEIGHT AND PERFORMANCE OF SOME ROTORCRAFT HAUV

Prototype	Nezha III [13]	Loon Copter [15]	Naviator [16]	Hydrone [17]	Morphable HAUV [18]	Berkeley [9]	Nezha-mini
Size	>1m	0.5-1m	0.5-1m	0.3-0.5m	0.5-1m	<0.3m	<0.3m
Weight	>10kg	2-5kg	2-5-kg	1-2kg	<1kg	<1kg	<1kg
Entire cycle	✓	✓	✓	×	✓	×	✓
Rapid transition	×	×	✓	×	×	×	✓

cope with is also more limited [9]. Hence, transition strategies for the miniaturized HAUV are necessary to be explored. Besides, the waterproofing and pressure resistance requirements increase the weight and volume. The carrying capacity of battery satisfies the endurance. However, the weight proportion of the power system is relatively large compared to other structures. These factors are all not conducive to the miniaturization and lightweight of HAUV.

A number of robotic platforms, such as the fixed wings, bionic microrobots and rotorcraft vehicles, have been developed to explore the multiphase locomotion. The fixed wings have higher requirements on the speed and attitude during the cross-domain locomotion [10]. In addition, although the weight of the fixed wings is light, the wingspan increases the size and is against miniaturization [11]. For bionic robots, their size is generally too microsized (millimeter-level in [8]), and the movement ability and range are limited so that there is still a certain distance from practical engineering application [12]. The rotorcrafts improve the stability of the miniaturized systems compared to fixed wings, but the additional motors and mechanical components generally increase the overall weight of the vehicle. For example, both Nezha [13], [14] and Loon Copter [15] adopt an additional buoyancy regulating mechanism that allows the mode switch during the transition. Whereas it sacrifices the rapidity of transition and enlarges the weight and volume. Naviator uses two sets of aerial propellers for both airborne and underwater propulsion (four propellers in each set), displaying good stability in both media, but the aerial propellers are less efficient in the water [16]. All the HAUVs above displayed the capacity of the entire cross-domain cycle in field tests. However, they do not meet the demand of miniaturization and lightweight relatively. In recent years, more teams have implemented the work on the miniature HAUV of new conceptions. The two HAUVs in [7], [17] have only completed simulation tests instead of experimental verification. The Mini HAUV from Berkeley weighs only 202 g and is 14 cm wide, which is the smallest rotorcraft HAUV at present. However, it has only completed the water-exit experiment [9].The morphable HAUV in [18] adopts vector propulsion underwater aided by a tilting mechanism. Detailed parameters about the size and weight are shown in Table I. Entire cycle indicates the capability of performing the whole water-air process while rapid transition refers to the the capability of transiting continuously without reliance on assistive mechanisms.

This letter reports a novel low-cost hybrid aerial underwater vehicle named Nezha-mini, which owns the same size as the A4 paper and weighs only 953 g. The modularity and encapsulation of the main components enhance the robustness of the configuration. The optimized thruster layout and the airframe structure permit the maneuverability comparable to that of a quadrotor in the flight mode and an autonomous underwater vehicle (AUV) in the underwater mode. Furthermore, a complete multi-phase control framework, comprising the transition strategy, was designed based on the compound dynamics model. The entire flight-submergence-flight cycle and the deep submergence were fulfilled in the field experiments, exhibiting high coincidence with the simulation results.

II. PROTOTYPE VEHICLE DESIGN

A. Configuration Overview

Nezha-mini opts for the carbon fiber airframe of the first-person view (FPV) drone, divided into two layers by the 15 mm aluminum columns. The lower bottom board extends to the bow for the vertical marine thruster (M1). The spacing between the bottom and top boards can accommodate a 4 in 1 waterproof aerial electronic speed controller (ESC) and allow the bow thruster M1 to be appropriately positioned. The top board holds four aerial thrusters (A1 to A4, anticlockwise) and the electronics bay (EE Bay), surrounded by a removable foam buoyancy material. The two outward-turning marine thrusters (M2 and M3) are symmetrically and horizontally fastened to the stern and are non-interacting with the buoyancy material and aerial thrusters. More details are shown in Fig. 2.

Nezha-mini is sized 280 × 193 × 91 mm (length, width, and height) without propellers, represented by $[L, W, H]$ respectively as shown in Fig. 3. The EE Bay is sized 237 × 45 × 2 mm (length, diameter, and thickness) and marked as $[L_{EE}, W_{EE}, H_{EE}]$. The buoyancy material is designed to ensure the body's center of buoyancy (C_B) and the center of gravity (C_G) are aligned vertically and C_B locates higher than C_G to allow the stability on the water surface. The distance from the designed waterline to the top of the buoyancy material is 3 mm. The whole HAUV weighs 953 g and the mass distribution is shown in Fig. 3. The two sets of thrusters improve the maneuverability in distinct media, but the trade-off is that the weight of the propulsion system is considerable, accounting for almost half of the total weight.

B. Avionics

Nezha-mini adopts two sets of microcontrollers for the locomotion in distinct media (Fig. 4). The flight controller is equipped with a GPS and a receiver (RC) communicating with the ground station, and leverages the available firmware of quadrotors. The inertial measurement unit (IMU) of the flight

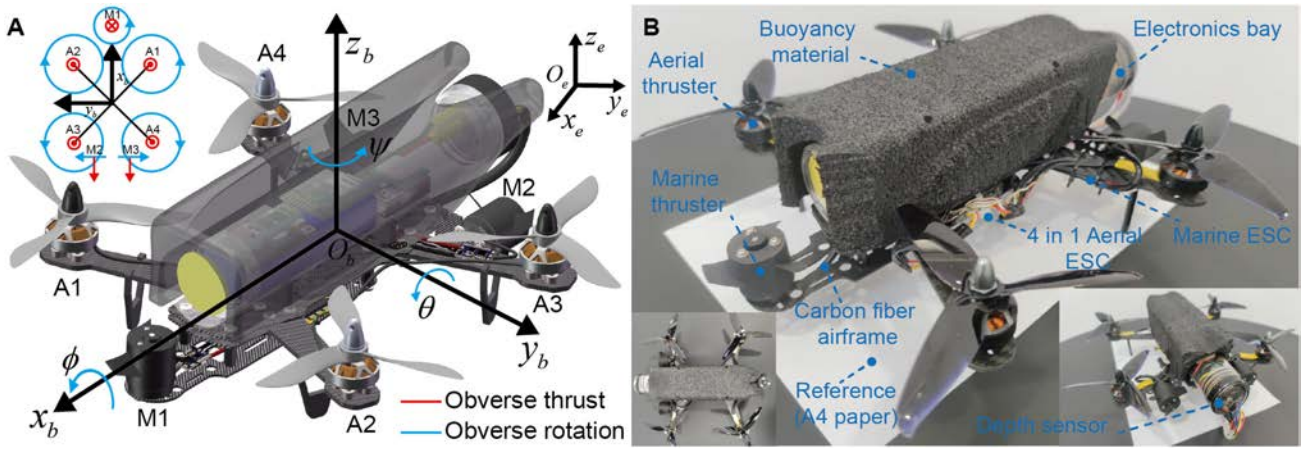

Fig. 2. **A.** Model of Nezha-mini with the marks on the coordinate systems and obverse directions. **B.** Three views of Nezha-mini and the marks of the main components.

Fig. 3. **A.** Four views of Nezha-mini and the marks of several principal dimensions. **B.** Mass distribution of Nezha-mini.

module is also embedded in the controller. The underwater controller integrates independent sensors, including the miniature IMU and depth sensor (MS5837). The former interacts with the controller through the USART communication protocol and the latter requires the I2C protocol. The controller runs the preprogrammed algorithms which are uploaded by the HC-06 Bluetooth module. The secure digital memory card (SD) records the navigation data and communicates through the SPI protocol with the controller. The controllers are powered by the 5 V voltage, converted from the 12.6 V voltage of the 3 s LiPo battery through a voltage regulator (Reg). Each electronic component is fed by the onboard 3.3 V voltage of the corresponding controller except for the high-powered HC-06 and SD modules. They are fed directly by the 5 V voltage of Reg to prevent the overheating of the main control board. All the electronic structures are encapsulated in an acrylic cylinder (EE Bay) to ensure water tightness, so the scale is also a restriction for selecting avionics except for the weight and power.

The ESCs are arranged outside the EE Bay and are waterproof, which facilitates the heat dissipation and saves the space of EE Bay. The power and signal bus (PSB) connects the internal and external EE Bay, and transmits seven channels of pulse width modulation (PWM) signals output by the controllers and the 12.6 V power for the ESCs. The PSB comes out of the rear cover of EE Bay and is connected to the aerial ESC. Besides, the depth sensor is also fixed to the boreholes in the rear cover. Thus, the rear cover is waterproof with epoxy resin.

III. Dynamics and Control

A. Multi-Modal Dynamics

The simplified geometric model of Nezha-mini is shown in Fig. 2. Two frames are defined: a frame attached to the static water surface $\{\boldsymbol{R_E}\}(O_e, x_e, y_e, z_e)$, which is the inertial frame, and a body-fixed frame $\{\boldsymbol{R_B}\}(O_b, x_b, y_b, z_b)$, where O_b is fixed on the center of mass of HAUV (C_G in Fig. 3). The position vector in $\{\boldsymbol{R_E}\}$ is defined as $\boldsymbol{\chi} = [x\ y\ z]^T$, and the attitude vector is defined as $\boldsymbol{\Theta} = [\phi\ \theta\ \psi]^T$. The velocity vector and angular rate vector in $\{\boldsymbol{R_B}\}$ are $\boldsymbol{\upsilon} = [u\ v\ w]^T$ and $\boldsymbol{\Omega} = [p\ q\ r]^T$ respectively. The rotation matrix $\{\boldsymbol{R_1}\}$ expressing the transformation from

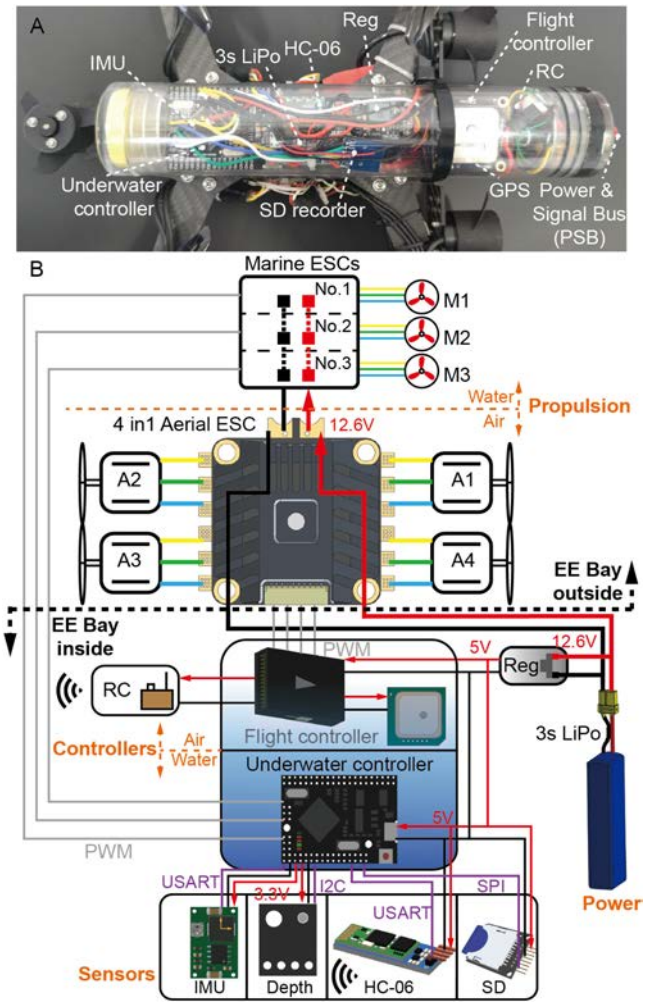

Fig. 4. **A.** Overview of the EE Bay layout. **B.** Electronic, electrical and hardware framework of Nezha-mini.

$\{\boldsymbol{R_B}\}$ to $\{\boldsymbol{R_E}\}$ and the transformation matrix of angular rate $\{\boldsymbol{R_2}\}$ are given by:

$$\boldsymbol{R_1} = \begin{bmatrix} c\theta c\psi & s\phi s\theta c\psi - c\phi s\psi & c\phi s\theta c\psi + s\phi s\psi \\ c\theta s\psi & s\phi s\theta s\psi + c\phi c\psi & c\phi s\theta s\psi - s\phi c\psi \\ -s\theta & s\phi c\theta & c\phi c\theta \end{bmatrix} \quad (1)$$

$$\boldsymbol{R_2} = \begin{bmatrix} 1 & s\phi t\theta & c\phi t\theta \\ 0 & c\phi & -s\phi \\ 0 & \frac{s\phi}{c\theta} & \frac{c\phi}{c\theta} \end{bmatrix} \quad (2)$$

where $c(\cdot)$, $s(\cdot)$ and $t(\cdot)$ denote $\cos(\cdot)$, $\sin(\cdot)$ and $\tan(\cdot)$ respectively. Notice that R_1 is an orthogonal matrix, so we have $\boldsymbol{R_1^{-1}} = \boldsymbol{R_1^T}$. Therefore, the kinematic equation of our HAUV is:

$$\dot{\boldsymbol{\chi}} = R_1 \boldsymbol{v},\ \dot{\boldsymbol{\Theta}} = R_2 \boldsymbol{\Omega} \quad (3)$$

To simplify the model, the coupling terms and higher-order terms are ignored. The multi-modal dynamics for the vehicle under $\boldsymbol{R_B}$ are given based on the Newton-Euler equation:

$$\begin{aligned} &(\boldsymbol{M_0} - k\boldsymbol{M_a})\dot{\boldsymbol{v}} - [(\boldsymbol{M_0} - k\boldsymbol{M_a})\boldsymbol{v}]\times\boldsymbol{\Omega} \\ &-k\boldsymbol{D_M}\boldsymbol{v}|\boldsymbol{v}| + \boldsymbol{g_1} = (1-k)\boldsymbol{F_{air}} + k\boldsymbol{F_{water}} \end{aligned} \quad (4)$$

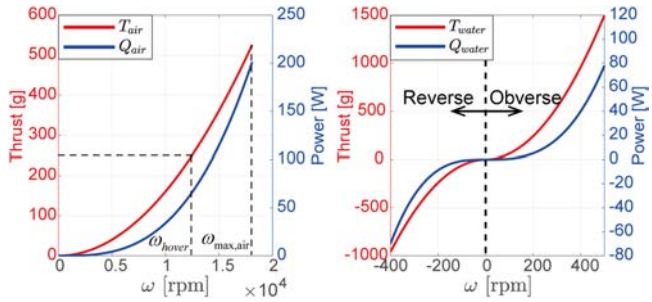

Fig. 5. The characteristic curves of (a) aerial thrusters and (b) marine thrusters.

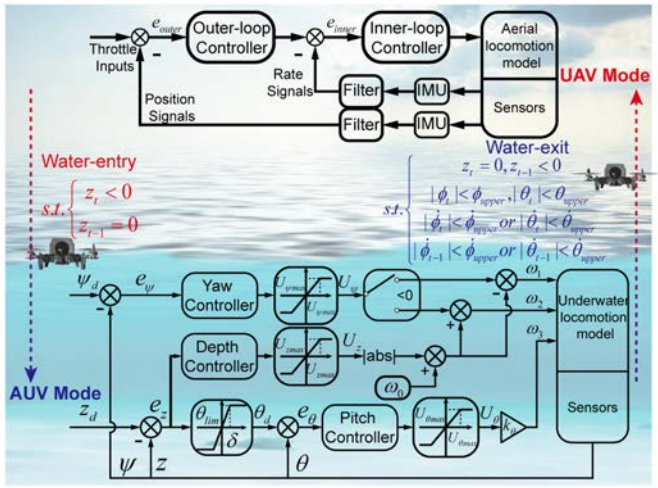

Fig. 6. Control strategies and cross-domain triggers of the complete and continuous cross-domain locomotion.

TABLE II
MODEL PARAMETERS OF NEZHA-MINI FROM THE ESTIMATION AND SYSTEM IDENTIFICATION

Symbol	Value & Unit
$[I_{xx}, I_{yy}, I_{zz}]$	[2.54,5.71,7.71]$\times 10^{-3}$kg·m^2
$[X_{\dot{u}}, Y_{\dot{v}}, Z_{\dot{w}}]$	[-0.29,-0.29,-0.49]kg
$[K_{\dot{p}}, M_{\dot{q}}, N_{\dot{r}}]$	[-0.5,-1.1,-2.3]$\times 10^{-3}$kg·m^2
$[X_{u\|u\|}, Y_{v\|v\|}, Z_{w\|w\|}]$	[-11.2,-11.2,-27.5]N·(m/s)$^{-2}$
$[K_{p\|p\|}, M_{q\|q\|}, N_{r\|r\|}]$	[-0.1,-0.2,-0.3]N·m·(m/s)$^{-2}$
$\boldsymbol{r_B} = [x_f\ y_f\ z_f]^T$	[0,0,18.5]^{T}mm
$\boldsymbol{r_{M1}}$	[140.3,0,-3]^{T}mm
$\boldsymbol{r_{M2}}$	[-97.3;54.5;-10]^{T}mm
$\boldsymbol{r_{M3}}$	[-97.3;-54.5;-10]^{T}mm

$$\begin{aligned} &(\boldsymbol{J_0} - k\boldsymbol{J_a})\dot{\boldsymbol{\Omega}} + (k\boldsymbol{M_a}\boldsymbol{v})\times\boldsymbol{v} - [(\boldsymbol{J_0} - k\boldsymbol{J_a})\boldsymbol{\Omega}]\times\boldsymbol{\Omega} \\ &-k\boldsymbol{D_J}\boldsymbol{\Omega}|\boldsymbol{\Omega}| + \boldsymbol{g_2} = (1-k)\boldsymbol{M_{air}} + k\boldsymbol{M_{water}} \end{aligned} \quad (5)$$

where,

1) (Added) Mass and Inertia: m is the mass of HAUV and $\boldsymbol{M_0} = diag[m, m, m]$. $\boldsymbol{J_0} = diag[I_{xx}, I_{yy}, I_{zz}]$ is the moment of inertia around the x, y, z axis of $\boldsymbol{R_B}$. $\boldsymbol{M_a} = diag[X_{\dot{u}}, Y_{\dot{v}}, Z_{\dot{w}}]$, $\boldsymbol{J_a} = diag[K_{\dot{p}}, M_{\dot{q}}, N_{\dot{r}}]$ are the added mass and inertia of the 6 degrees of freedom (6DOF) in hydrodynamics. The estimated values are shown in Table II.

2) Damping: The drag coefficients and drag moment coefficients are expressed as $\boldsymbol{D_M} = diag[X_{u|u|}, Y_{v|v|}, Z_{w|w|}]$ and

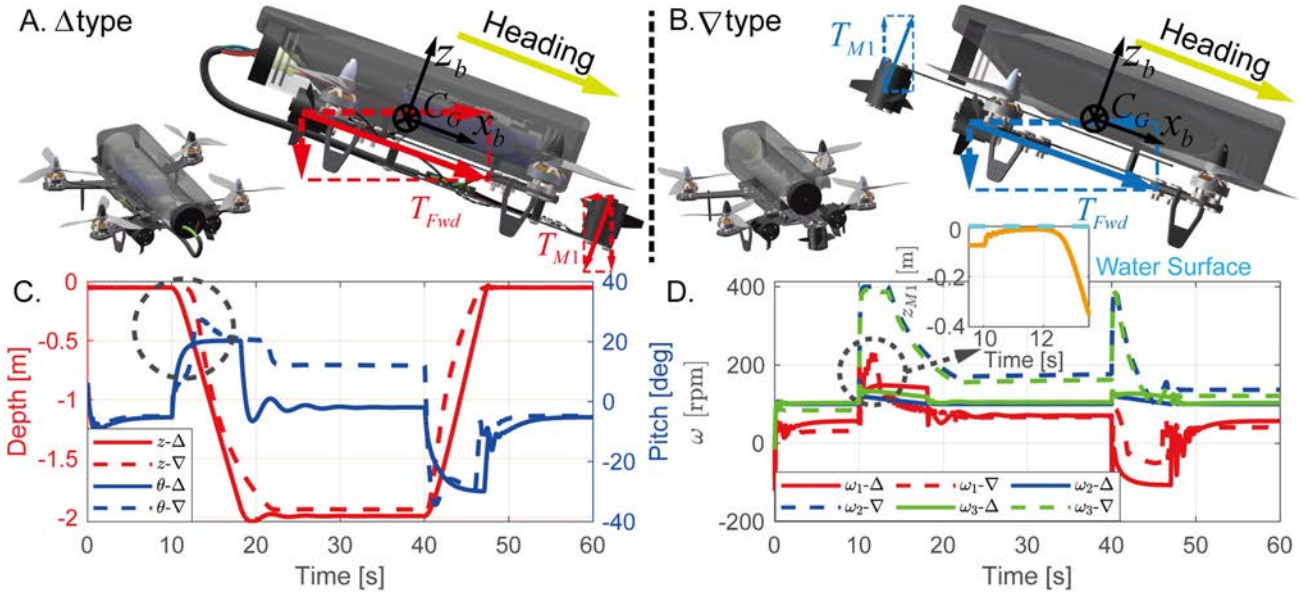

Fig. 7. Comparison of the two design schemes: **A.** Δ type and **B.** ∇ type. **C.** Simulation results of depth and pitch channels of the two types. **D.** Simulation results of the thruster speeds of the two types (ω_1 to ω_3 are indicated as the speed of M1 to M3).

$\boldsymbol{D_J} = diag[K_{p|p|}, M_{q|q|}, N_{r|r|}]$ in 6DOF respectively. They can be estimated through system identification.

3) Restoring Force and Moment: Let the gravity vector of HAUV be $\boldsymbol{f_G} = [0\ 0\ -mg]^T$, and the buoyancy vector is $\boldsymbol{f_B} = [0\ 0\ \rho_{water} gV]^T$, where g=9.8 m/s ^{2} is the acceleration of the gravity, ρ_{water}=1000 kg/m^3 is the density of water and V=9.72×10^{-4} m^3 is the volume of Nezha-mini. In addition, let the coordinates of the center of buoyancy in $\{\boldsymbol{R_B}\}$ (C_B in Fig. 3) be $\boldsymbol{r_B} = [x_f\ y_f\ z_f]^T$ when the HAUV is fully submerged, so we have: $\boldsymbol{g_1} = -\boldsymbol{R_1^T}(\boldsymbol{f_B} + \boldsymbol{f_G})$ and $\boldsymbol{g_2} = -\boldsymbol{r_B} \times \boldsymbol{R_1^T} \boldsymbol{f_B}$.

4) Control Force and Moment: The thrust model of propellers can be written as follows.

$$\begin{aligned} T_{ji} &= \rho_j C_{Tj}(J) \omega_{ji}^2 D_j^4, \\ Q_{ji} &= \rho_j C_{Qj}(J) \omega_{ji}^3 D_j^5, \\ M_{ji} &= \frac{Q_{ji}}{\omega_{ji}},\ i = 1, 2, 3, (4),\ j = A(air), M(water) \end{aligned} \quad (6)$$

where, ρ_{air}=1.29 kg/m^3 is the density of air. T_{ji}, Q_{ji} and M_{ji} are the thrust, power and torque generated by A1 to A4 or M1 to M3. C_{Tj} and C_{Qj} are the thrust coefficients and power coefficients in air or water, which is related to the coefficient of advanced velocity J. ω_{ji} is the propeller speed and D_j is the diameter of the aerial and marine propellers. Define d_j as the ratio of C_{Qj} to C_{Tj}, so we have $M_{ji} = T_{ji} d_j$. The fitted static characteristic curves of the thrusters are given in Fig. 5 based on (6). Since the vehicle operates at low speed, we ignore the influence of J on the curves.

The origins of coordinates of M1 to M3 are marked as C_{M1} to C_{M3} in Fig. 3. Their position vectors to C_G are denoted as $\boldsymbol{r_{M1}}$ to $\boldsymbol{r_{M3}}$. The underwater model can be expressed as:

$$\begin{aligned} \boldsymbol{F_{water}} &= [T_{M2} + T_{M3}, 0, T_{M1}]^T, \\ \boldsymbol{M_{water}} &= \boldsymbol{r_{M1}} \times [0, 0, T_{M1}]^T + \boldsymbol{r_{M2}} \times [T_{M2}, 0, 0]^T \\ &\quad + \boldsymbol{r_{M3}} \times [T_{M3}, 0, 0]^T + [0, 0, M_{M1}]^T \end{aligned} \quad (7)$$

Furthermore, the normal direction of the vertical thruster M1 is orthogonal to the advanced orientation of the vehicle, resulting in the curved streamlines and thus thrust loss, which can be modeled by the empirical formula (8) summarized in [19].

$$T_{M1} = 1.078 e^{-1.654\,u} \rho_{water} C_{Twater}(J) \omega_{M1}^2 D_{water}^4 \quad (8)$$

where u is the speed in x_b axis.

The centers of A1 to A4 deviate little from C_G, so that we assume that they coincide. The aerial model follows the general thrust distribution principle for quadrotors:

$$\begin{aligned} \boldsymbol{F_{air}} &= \left[0, 0, \sum_{i=1}^{4} T_{Ai}\right]^T,\ \boldsymbol{M_{air}} \\ &= \begin{bmatrix} -\frac{\sqrt{2}}{2} L_A & \frac{\sqrt{2}}{2} L_A & \frac{\sqrt{2}}{2} L_A & -\frac{\sqrt{2}}{2} L_A \\ -\frac{\sqrt{2}}{2} L_A & -\frac{\sqrt{2}}{2} L_A & \frac{\sqrt{2}}{2} L_A & \frac{\sqrt{2}}{2} L_A \\ -d_{air} & d_{air} & -d_{air} & d_{air} \end{bmatrix} \begin{bmatrix} T_{A1} \\ T_{A2} \\ T_{A3} \\ T_{A4} \end{bmatrix} \end{aligned} \quad (9)$$

where L_A =124 mm is the length of the arm of airframe.

Lastly, k is the phase factor that $k = 1$ means the underwater state and $k = 0$ means the airborne state.

B. Control Strategies and Cross-Domain Triggers

Similar to the typical quadrotors, Nezha-mini operates in UAV mode with an inner and outer closed-loop control logic as shown in Fig. 6, with the outer loop tracking the position and the inner loop tracking the rate, and the output of the outer loop serving

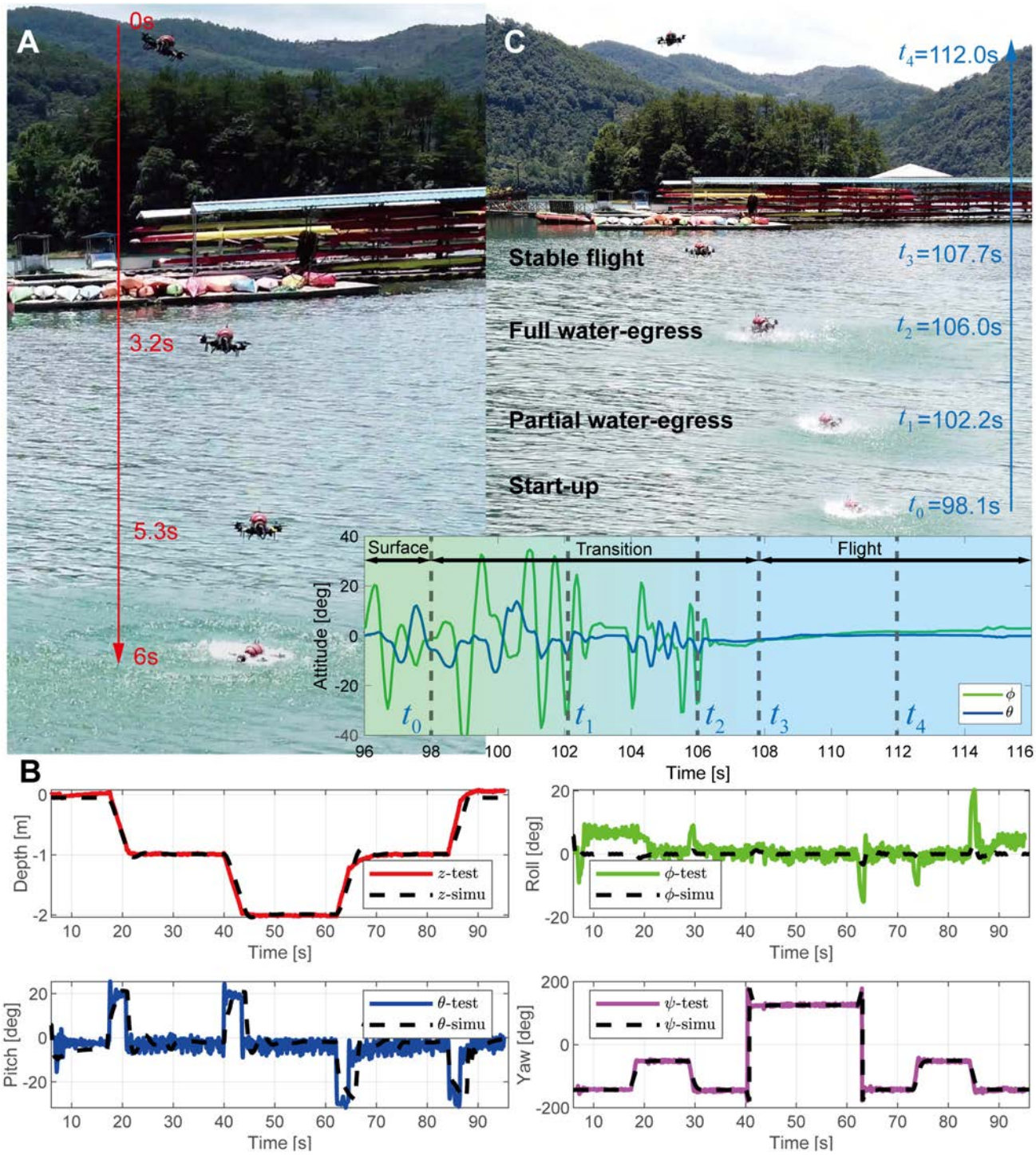

Fig. 8. Complete cross-domain mission cycle (Flight-submergence-flight): (A) Landing on the water surface after the first flight. (B) Simulation and experimental results of the depth and attitude of the underwater maneuvering locomotion. (C) Trigger of the window period (t_0) and the whole process of the water-egress.

as the input of the inner loop [20]. When operating in AUV mode, Nezha-mini is a severely underactuated system which is not capable of diving vertically and moving sideways. The prerequisite for all underwater locomotion is the slow advance of the vehicle, which requires the idling of the rear thrusters M2 and M3 with the speed ω_0. On this basis, M1 operates forward or backward to fulfill the descending and ascending with the desired pitch angle θ_{lim} through a double closed-loop strategy, and the course is altered through the differential rotation of M2 and M3. U_z, U_θ, U_ψ are respectively the output of the controller of the depth, pitch and yaw channels after the amplitude clipping, and are mixed to get the thruster speeds subsequently. The speed limitations of each channel are $U_{zmax}, U_{\theta max}, U_{\psi max}$. Moreover, for decoupling the depth and pitch channel, δ is introduced,

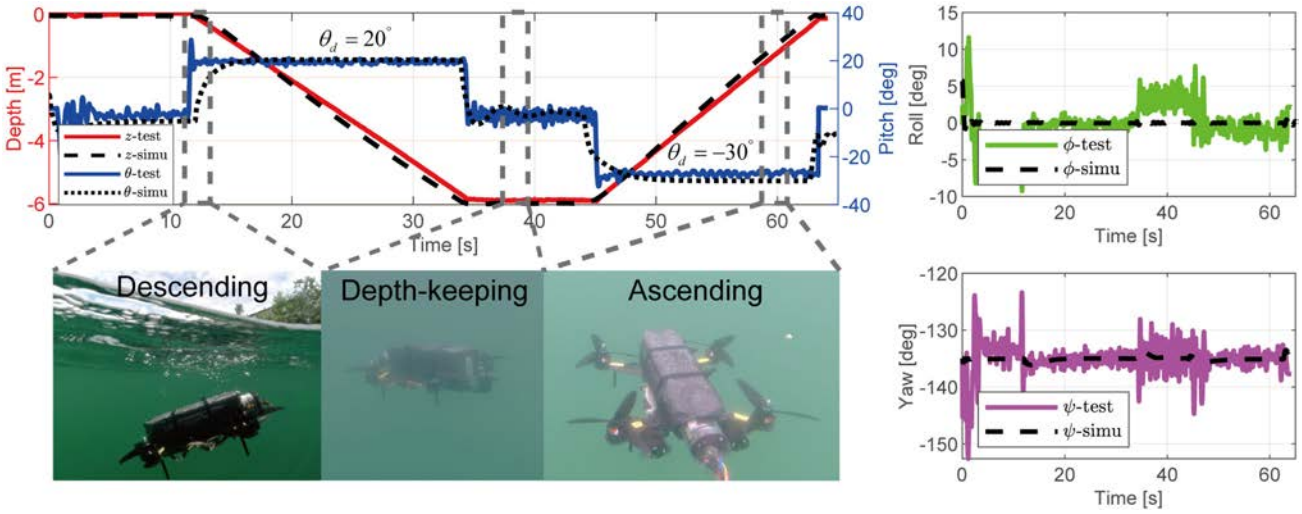

Fig. 9. Automatic underwater locomotion of the depth-keeping and head-keeping.

which is the fluctuating interval of the desired depth z_d. When z approaches z_d (within the interval δ), both the advanced speed and pitch angle are decreased to make the system converge as steadily as possible. To reduce the computational complexity and ensure stability, the cascade proportional-integral-differential (PID) controller is used in each channel.

A complete real-time triggering mechanism is proposed to guarantee continuous and rapid cross-domain locomotion without neglecting the system's stability. During the transition period, the HAUV will inevitably encounter wave disturbance resulting in attitude fluctuations. Therefore, it is necessary to find a relatively small and stable moment of attitude as the take-off window. The window satisfies the following four conditions simultaneously and the mathematical expression is shown in Fig. 6.

1) Depth limitation: The HAUV has surfaced.
2) Attitude limitation: Attitude is small at this moment.
3) Tendency limitation: Attitude approaches a minimum.
4) Stability assurance: Attitude change is not apparent.

In contrast, the water-entry trigger is more straightforward, requiring just launching M1 to M3 and shutting down A1 to A4 after the depth sensor detects the vehicle falling into the water, without considering the attitude stability.

IV. Actuation Layout Consideration

The overall actuation layout of Nezha-mini is defined as the "X+Δ" type. A1 to A4 adopts the traditional X-shaped layout of quadrotors relative to O_b. However, the layout of M1 to M3 is worth considering. The vertical thrusters of some three-propeller-driven vehicles are embedded in the middle of the fuselage near C_G to achieve the vertical heave [21]. But this will lead to a discontinuous fuselage and is not beneficial for miniaturization. Therefore, two options were considered in the design: bow-mounted vertical thrusters (Δ type and) and stern-mounted vertical thrusters (∇ type), as shown in Fig. 7. We assume that the difference between the two schemes is only in the location of M1 ($\boldsymbol{r}_{M1\nabla} = -\boldsymbol{r}_{M1\Delta}$), and ignore the interaction of the thrusters' flow field. Based on the dynamic model proposed in Section III, the underwater simulation is carried out in Fig. 7(c) and (d).

Intuitively, the stress analysis in Fig. 7(a) and (b) shows that the perpendicular component of the control force of pitch T_{M1} and the propulsive force T_{Fwd} is reinforcing of the Δ type while restraint of the ∇ type, which indicates that higher RPM is required to achieve the same diving speed than the former (about 8 times of ω_2, ω_3 when diving and 1.7 times when navigating in Fig. 7(d)). Meantime, the relation between speed and power is cubic according to (6). Therefore, ∇ type is significantly detrimental to the power consumption. The same analysis applies to the surfacing period.

On the other hand, the stern-mounted M1 will be lifted in the initial diving and is possible to be exposed to the air. The vehicle may fail to dive due to the failure to reach the suitable pitch angle because of the thrust loss and restoring moment, while the Δ type is not confused by this problem. We assume that the thrust decays linearly from C_G to the water surface. The subfigure in Fig. 7(d) describes the response of z_{M1}, the distance between M1 and the surface, which causes a dive lag and significant overshoot in pitch and RPM (the black circle in Fig. 7). Above all, we adopted the Δ type for the layout of the underwater actuation.

V. Validation: Simulations and Experiments

A. Multi-Domain Locomotion Cycle

Outdoor experiments were performed to assess the robot's entire capacity of the multi-domain locomotion: stable flight, underwater maneuverability and rapid transition, as shown in Fig. 8. Nezha-mini landed on the water surface within 6 s after the first flight mission and subsequently triggered the preassigned grid locomotion within 0 m to -2 m. θ_d for the descending and ascending was 20 degrees and -30 degrees respectively. The fluctuation of the pitch response during the depth-keeping period

was within 5 degrees and the depth error was within 5 mm. The turning radius at the current speed can be approximately estimated by the diving speed (about 0.3 m/s) and attitude, which was about 0.38 m. The simulated and experimental results coincided well and showed accurate tracking performance. The roll channel responded to large fluctuations when turning the course, which is not apparent in the simulation. After surfacing, the vehicle did not start until the prediction conditions in Fig. 6 of the window period (t_0) reacted. The transition lasted about 9 s and the robot experienced multiple attitude vibrations, accompanied by the aerial propellers slamming against the mixed media intermittently (t_1). The secondary flight mission proceeded (t_3 to t_4) after the full water-egress (t_2). It is worth noticing that spare buoyancy material was used for the whole process, reflecting strong adaptability and robustness of Nezha-mini.

B. Deep Submergence

The deep submergence was also carried out. The maximum depth of diving reached 6 m due to the depth limitation of the experimental site. It can be calculated from Fig. 9 that the descending and ascending speed are evenly about 0.25 m/s and 0.32 m/s under the 30% throttle propulsion and the preset θ_d. The maximum jitter of roll and yaw is about 10 degrees. The experimental results of depth and pitch channels are in good agreement with the simulation results. We used safety cables in case of emergency at the deep submergence case. Video attachment: https://www.bilibili.com/video/BV1ju411k7Jy/

VI. Conclusion

In this letter, the design concept for Nezha-mini, a miniaturized, lightweight and low-cost HAUV, is presented. The four X-layout aerial thrusters and the unique underwater propulsion module qualify the potential of performing complete multi-phase maneuverability and rapid cross-domain reaction. Additionally, the multi-modal dynamics and control framework are proposed to validate and further implement the prototype test. Meanwhile, the cross-domain trigger is given for the prediction of the window period of the more stable water-egress. Moreover, the layout of the underwater thrusters is optimized in terms of power consumption and controllability through the simulation. The entire multi-domain locomotion cycle and deep submergence were achieved in the field experiments and the tracking performance of both flight and underwater controllers in depth and attitude channel approached the simulation results. The developed robot will be effective and low-cost for applications such as the sampling of the water-air interface and the detection of intensive obstacle areas, as compared to the current multi-vehicle solutions.

In the future, the control framework will be extended to achieve the fully autonomous takeoff in consideration of the water-air mixed domain and compound disturbance. Further weight reduction will be explored. Additionally, a miniature navigational sensor is in development to accurately track the horizontal degree of freedom. Finally, pushing this platform of the current scale level towards the orientation of clustering and synergy is our long-term envisagement.

References

[1] B. Hadi, A. Khosravi, and P. Sarhadi, "A review of the path planning and formation control for multiple autonomous underwater vehicles," *J. Intell. Robotic Syst.*, vol. 101, no. 4, pp. 1–26, 2021.

[2] D. I. Koutras, A. C. Kapoutsis, and E. B. Kosmatopoulos, "Autonomous and cooperative design of the monitor positions for a team of UAVs to maximize the quantity and quality of detected objects," *IEEE Robot. Automat. Lett.*, vol. 5, no. 3, pp. 4986–4993, Jul. 2020.

[3] B. Anja, G. Vasiljevic, and N. Miskovic, "Vehicle-in-the-loop framework for testing long-term autonomy in a heterogeneous marine robot swarm," *IEEE Robot. Automat. Lett.*, vol. 5, no. 3, pp. 4439–4446, Jul. 2020.

[4] E. M. Fischell, A. R. Kroo, and B. W. O'Neill, "Single-hydrophone low-cost underwater vehicle swarming," *IEEE Robot. Automat. Lett.*, vol. 5, no. 2, pp. 354–361, Apr. 2020.

[5] D. Debruyn *et al.*, "MEDUSA: A multi-environment dual-robot for underwater sample acquisition," *IEEE Robot. Automat. Lett.*, vol. 5, no. 3, pp. 4564–4571, Jul. 2020.

[6] X. Yang, T. Wang, J. Liang, G. Yao, and M. Liu, "Survey on the novel hybrid aquatic–aerial amphibious aircraft: Aquatic unmanned aerial vehicle (AquaUAV)," *Prog. Aerosp. Sci.*, vol. 74, pp. 131–151, Apr. 2015.

[7] A. Vyas, R. Puppala, N. Sivadasan, A. Molawade, T. Ranganathan, and A. Thondiyath, "Modelling and dynamic analysis of a novel hybrid aerial–underwater robot-Acutus," in *Proc. OCEANS 2019-Marseille*, 2019, pp. 1–6.

[8] Y. Chen *et al.*, "A biologically inspired, flapping-wing, hybrid aerial-aquatic microrobot," *Sci. Robot.*, vol. 2, no. 11, 2017, Art. no. eaao5619.

[9] J. Zha, E. Thacher, J. Kroeger, S. A. Mäkiharju, and M. W. Mueller, "Towards breaching a still water surface with a miniature unmanned aerial underwater vehicle," in *Proc. 2019 Int. Conf. Unmanned Aircraft Syst.*, 2019, pp. 1178–1185.

[10] W. Weisler, W. Stewart, M. B. Anderson, K. J. Peters, A. Gopalarathnam, and M. Bryant, "Testing and characterization of a fixed wing cross-domain unmanned vehicle operating in aerial and underwater environments," *IEEE J. Ocean. Eng.*, vol. 43, no. 4, pp. 969–982, Dec. 2017.

[11] R. Zufferey *et al.*, "Sailmav: Design and implementation of a novel multi-modal flying sailing robot," *IEEE Robot. Automat. Lett.*, vol. 4, no. 3, pp. 2894–2901, Jun. 2019.

[12] R. Siddall and M. Kovač, "Launching the AquaMAV: Bioinspired design for aerial–aquatic robotic platforms," *Bioinspiration Biomimetics*, vol. 9, no. 3, 2014, Art. no. 031001.

[13] D. Lu *et al.*, "Design, fabrication, and characterization of a multi-modal hybrid aerial underwater vehicle," *Ocean Eng.*, vol. 219, 2021, Art. no. 108324.

[14] C. Lyu *et al.*, "Toward a gliding hybrid aerial underwater vehicle: Design, fabrication, and experiments," *J. Field Robot.*, pp. 1–14, 2022.

[15] H. Alzu'bi, I. Mansour, and O. Rawashdeh, "Loon copter: Implementation of a hybrid unmanned aquatic–aerial quadcopter with active buoyancy control," *J. Field Robot.*, vol. 35, no. 5, pp. 764–778, Aug. 2018.

[16] M. M. Maia, D. A. Mercado, and F. J. Diez, "Design and implementation of multirotor aerial-underwater vehicles with experimental results," in *Proc. IEEE/RSJ Int. Conf. Intell. Robots Syst.*, 2017, pp. 961–966.

[17] A. A. Neto, L. A. Mozelli, P. L. J. Drews, and M. F. M. Campos, "Attitude control for an hybrid unmanned aerial underwater vehicle: A robust switched strategy with global stability," in *Proc. IEEE Int. Conf. Robot. Automat.*, 2015, pp. 395–400.

[18] Y. H. Tan and B. M. Chen, "A morphable aerial-aquatic quadrotor with coupled symmetric thrust vectoring," in *Proc. IEEE Int. Conf. Robot. Automat.*, 2020, pp. 2223–2229.

[19] X. Xiang, C. Yu, Q. Zhang, P. A. Wilson, and G. Xu, "Manoeuvring-based actuation evaluation of an AUV with control surfaces and through-body thrusters," *Appl. Ocean Res.*, vol. 96, 2020, Art. no. 102046.

[20] Y. Bi, D. Lu, Z. Zeng, and L. Lian, "Dynamics and control of hybrid aerial underwater vehicle subject to disturbances," *Ocean Eng.*, vol. 250, 2022, Art. no. 110933.

[21] Z. Xu, M. Haroutunian, A. J. Murphy, J. Neasham, and R. Norman, "A comparison of functional control strategies for underwater vehicles: Theories, simulations and experiments," *Ocean Eng.*, vol. 215, 2020, Art. no. 107822.